Powder Technology 428 (2023) 118859

Contents lists available at ScienceDirect

Powder Technology

journal homepage: www.journals.elsevier.com/powder-technology

Flow regimes and characteristics of dense particulate flows with coarse particles in inclined pipe

Yan Zhang [a], Wanlong Ren [a,b], Peng Li [a], Xuhui Zhang [a,b,*], Xiaobing Lu [a,b]

[a] Institute of Mechanics, Chinese Academy of Sciences, Beijing, 100190, China
[b] School of Engineering Science, University of Chinese Academy of Sciences, Beijing, 100049, China

GRAPHICAL ABSTRACT

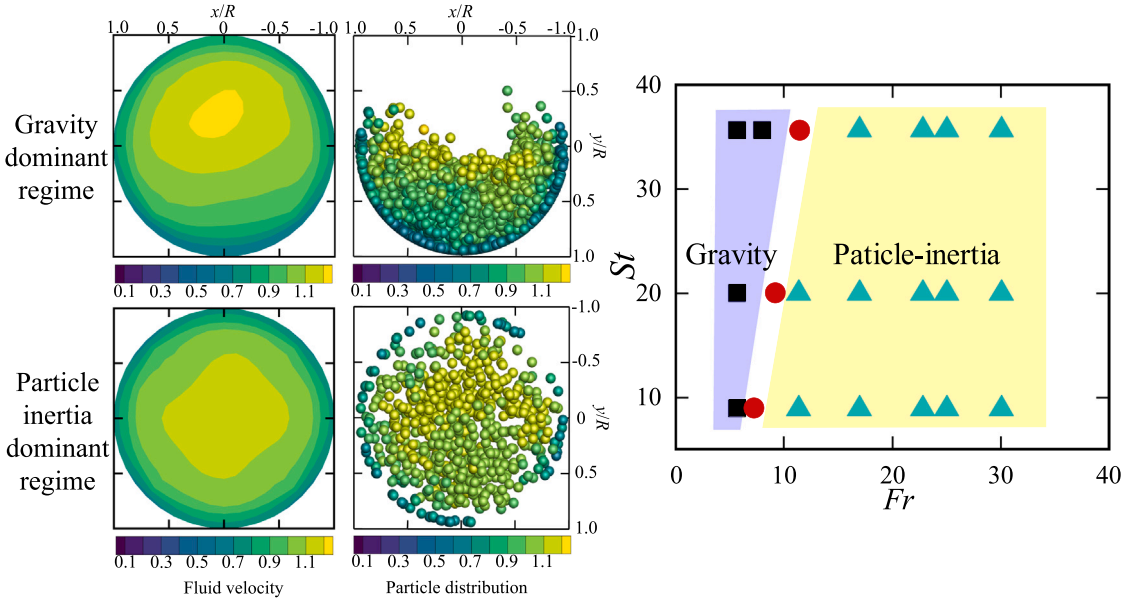

HIGHLIGHTS

- An optimized CFD-DEM is used to investigate dense particulate flows in inclined pipe.
- The flow regimes and their transitions of dense particulate flows in inclined pipe are analyzed.
- A new phase diagram for recognizing different flow regimes is given.
- Temporal variations of particle quantities are analyzed to illustrate propagating of kinematic waves.

ARTICLE INFO

Keywords:
Flow regimes
CFD-DEM

ABSTRACT

This paper presents a numerical simulation for dense particulate flows with coarse particles in inclined pipe to identify different flow regimes by means of computational fluid dynamics-discrete element method. The drag, gravitational, pressure gradient and virtual mass forces on particles, as well as the effect of particle–particle

* Corresponding author at: Institute of Mechanics, Chinese Academy of Sciences, Beijing, 100190, China.
E-mail address: zhangxuhui@imech.ac.cn (X. Zhang).

https://doi.org/10.1016/j.powtec.2023.118859
Received 10 May 2023; Received in revised form 8 July 2023; Accepted 30 July 2023
Available online 2 August 2023

Particulate flows
Inclined pipe
Coarse particles

collisions are considered. Two flow regimes and their transitions are observed and described. The influence of Stokes number St, Froude number Fr, inclination angle β, etc., on critical flow regimes is analyzed to identify the dependence of flow regimes on these parameters. A new diagram for recognizing regime transition is given. The temporal variations of flow fields are also analyzed to illustrate propagating of kinematic waves. The wave velocity increases with Fr, β, and particle concentration increasing. Two dimensionless numbers, collision stress and fluid–particle interaction stress, are defined to explain the regime transition mechanism. The maximum pressure drop occurs at approximately $\beta = 60°$.

1. Introduction

Dense particulate flows with coarse particles in pipeline are widely encountered in an array of industries in the civil, chemical, food, mining, and process industries [1–4]. For example, the poly-metallic nodules transport from the ocean bottom to the surface is the key process in deep-sea mining [5], where the internal flow is characterized as large particle size and high particle concentration (>5% volume/volume) [6,7]. According to Cunez et al. [8] and Zhang et al. [7], different flow instabilities and patterns have been identified for the dense particulate flows with coarse particles (d/D ~O(0.1)), where d/D is the ratio of particle diameter to pipe diameter, such as the plug, kinematic wave, and jamming may occurring. A key feature of the dense particulate flows with coarse particles in pipeline is that different flow regimes occur along the pipe. Generally, flow regimes are affected by a wide variety of factors, such as the particle concentration, particle and fluid properties, particle size, as well as particle–fluid and particle–particle interactions [9]. For example, dense particulate flows in vertical pipe often run in the form of suspension flow or dense-dilute flow, which results from the kinematic waves [10], because the flow direction is opposite to the gravity direction. The flow regimes in horizontal pipe may transit from the stationary-bed flow to the moving bed flow, and finally to the suspension flow as the conveying velocity increases [11]. The flow characteristics of different flow regimes are distinct, subsequently lead to different performance with regards to wall abrasion, particle degradation, and conveying efficiency.

Several previous investigations, both theoretically or experimentally, have been undertaken on the dense particulate flows in horizontal and vertical pipe. For example, Ravelet et al. [12] and Vlasák et al. [13] investigated the pressure drop of the sand-water mixtures in a horizontal pipe. The relationship between the hydraulic gradient and the mixture velocities was obtained. It was found that the pressure drop in horizontal pipe is higher than vertical pipe. Zhou et al. [11] thoroughly investigated the flow regimes and their transitions of dense particulate flows in horizontal pipe based on computational fluid dynamics-discrete element method (CFD-DEM). A new phase diagram in terms of the forces acting on particles was proposed for identifying the flow regimes. Some theoretical models, such as two-layer model [14] and the three-layer model [15], were proposed to describe the flow regimes. For dense particulate flows in vertical pipe, many researchers pay attention to the settling velocity of particle clusters [16], the two-phase distribution [17], and the particle shape effects [18]. However, a relatively little research has been taken on the dense particulate flows with coarse particles, especially in inclined pipes. The inclined pipe may be encountered in may situations, such as the hydraulic conveying of nodules in deep-sea mining, sewage treatment, etc. Predictably, gravity also plays an important role in the flow behavior for dense particulate flows in inclined pipes. Compared with the horizontal pipe, the flow regimes may undergo moving bed flow and suspension flow with the fluid velocity increasing. In addition, compared with the vertical pipe, the suspension flow may also have dense-dilute flow regime (or the kinematic waves) because the component of gravity along the pipe axial direction is the same as the flow direction. Therefore, the dense particulate flows in inclined pipe will have the motion characteristics of horizontal pipe and vertical pipe at the same time. It is of great importance to investigate dense particulate flows with coarse particles in inclined pipes.

For the experimental study of dense particulate flows in inclined pipe, Klinzing et al. [19] studied the pressure drop and particle velocity in the inclined pipe and found that the pressure drop increased with the increase in inclination angle (0–45°). Levy et al. [20] found that the pressure drop initially increased and then decreased with the inclination angle increasing from 0 to 90°, where the maximum pressure drop occurred at approximately 60°. Vlasak et al. [21] investigated the coarse particle-water mixture flow in inclined pipe. For moderate fluid velocities, particle saltation became the dominant mode of transportation. When the inclination angle is small (<30°), the effect of inclination on local particle concentration distribution is not significant. Two-phase slurry flow with sand concentrations ranging from 0.1% to 5% was studied in inclined pipe section using the video recordings by Archibong-Eso et al. [22]. Disperse (heterogeneous and homogeneous) and moving bed were observed. There existed a critical value of the particle concentrations for the pressure gradient, below which the pressure gradient reduced with a reduction in fluid velocity and above which the pressure gradient increased with a further reduction in fluid velocity. The measurements of the behavior of the fluid and particles are much more complex than measurements of only flow parameters, such as the flow rates, the pressure drop, and the overall particle concentration, especially with high particle concentration and large particle size. Due to the experimental challenges, the dense particulate flows with coarse particles in inclined pipe are not fully captured.

Researchers have also proposed various numerical models to study the characteristics of dense particulate flows, which can be classified into three categories [23]: macroscale, mesoscale, and microscale. Corresponding approaches are two-fluid model (TFM) [24], CFD-DEM [11], particle-resolved simulations (PRS) [25], etc. For example, Yang et al. [26] investigated the effects of fluid velocity, particle volumetric concentration and pipe inclination angle on the pressure drop and transport capacity of the pipeline based on CFD-DEM. The pressure drop increases slowly with the inclination angle increasing from 0 to 60°, but increases rapidly when the inclination angle increases from 60° to 90°. The lowest value of the transport capacity occurs at the inclination angle of 45° to 60°. Zhang et al. [27], Chen et al. [28] and Zhou et al. [29] used the CFD-DEM approach for studying the particle erosion of hydraulic bends. Obviously, above experiment and simulation researches show that the pipe inclination greatly affects the pressure drop. However, little research pays attention to the flow regimes and characteristics of the dense particulate flows in inclined pipe. From the experiment of Archibong-Eso et al. [22], suspension flow and moving bed flow were observed in inclined pipe, which is similar to the horizontal pipe. The dense particulate flows in inclined pipes need to be investigated to achieve design criteria for the transportation of solid particles and accuracy of energy loss. One of the objectives of the present work is to study the flow regimes of dense particulate flow with coarse particles in inclined pipe. Another objective is to discuss the influence of controlling parameters, such as the pipe inclination angle, the particle volume fraction, etc., on the flow characteristics because the absence of a systematic investigation prevents the different influences of these parameters from being well understood. In addition, as described above, the dense particulate flows in inclined pipe are similar to that in vertical pipe. We will also investigate the kinematic waves during the transportation process. The pressure drop under different controlling parameters will also be studied due to its importance for engineering application.

In summary, limited information is available that isolated the influence of controlling parameters on flow characteristics in dense particulate flows within inclined pipe. In this paper, we use an optimized CFD-DEM, which is suitable for coarse particles, to investigate this process. We aim to (1) identify the various regimes, (2) give the diagram for different regimes, (3) analyze the key characteristics of the two-phase behavior in each regime, (4) identify the kinematic waves of the two-phase flow, and (5) investigate the pressure drop of the two-phase flow. The remainder of this paper is as follows: in Section 2, the governing equations of the optimized CFD-DEM are introduced, which includes the submodels in the interphase coupling. The numerical setup and the model validation are also given. In Section 3, we analyze the flow regimes, the flow behavior and the particle dynamics. Section 4 summarizes the main findings.

2. Methods

2.1. Governing equations of the CFD and DEM

The fluid phase is described by the locally averaged variables over the computational mesh, where the continuity and momentum conservation of an incompressible fluid are solved [30]

$$\frac{\left(\partial \rho_f \alpha_f\right)}{\partial t} + \nabla \cdot \left(\rho_f \alpha_f \boldsymbol{u}\right) = 0 \,, \tag{1}$$

$$\frac{\partial \left(\rho_f \alpha_f \boldsymbol{u}\right)}{\partial t} + \nabla \cdot \left(\rho_f \alpha_f \boldsymbol{u}\boldsymbol{u}\right) = -\alpha_f \nabla p - \boldsymbol{F}_{pf} + \alpha_f \nabla \cdot \boldsymbol{\tau} + \rho_f \alpha_f \boldsymbol{g} \,, \tag{2}$$

where $\boldsymbol{u}$ and $\boldsymbol{g}$ are the vectors of the fluid phase velocity and the gravitational acceleration, respectively. α_f indicates the void fraction or the fluid volume fraction. p denotes the pressure. $\boldsymbol{F}_{pf}$ is the interphase momentum exchange term. $\boldsymbol{\tau}$ is the viscous stress of the fluid phase, which is expressed as

$$\boldsymbol{\tau} = \nu_f \left(\nabla \boldsymbol{u} + \nabla \boldsymbol{u}^{\mathrm{T}}\right) - \frac{2}{3}\nu_f \nabla \cdot \boldsymbol{u}\boldsymbol{\delta} \,, \tag{3}$$

where ν_f is the fluid viscosity, and $\boldsymbol{\delta}$ is the Kronecker delta. The interphase momentum exchange is written as

$$\boldsymbol{F}_{pf} = \frac{1}{V_c}\sum_{i=1}^{n}\left(\boldsymbol{f}_{d,i} + \boldsymbol{f}_{vm,i}\right) \,, \tag{4}$$

where V_c is the cell volume, n is the number of particles in a cell, $\boldsymbol{f}_{d,i}$ is the drag force fluid exert on particles, $\boldsymbol{f}_{vm,i}$ is the virtual mass force. In dense particulate flows, drag force, the pressure gradient force, and the virtual mass force are important. The pressure gradient term in Eq. (2) is multiplied by the void fraction to represent the effect of the pressure gradient force [31]. Hence, the interphase momentum exchange term in Eq. (4) does not contain the pressure gradient force.

The motion of the particle has translational and rotational forms, which is governed by Newton's second law and given by

$$m_i \frac{\mathrm{d}\boldsymbol{v}_i}{\mathrm{d}t} = \boldsymbol{f}_{pf,i} + \sum_{j=1}^{k_c}\boldsymbol{f}_{c,ij} + m_i \boldsymbol{g} \,, \tag{5}$$

$$I_i \frac{\mathrm{d}\boldsymbol{\omega}_i}{\mathrm{d}t} = \sum_{j=1}^{k_c}\boldsymbol{M}_{ij} \,, \tag{6}$$

where $\boldsymbol{v}_i$, m_i, $\boldsymbol{\omega}_i$, and I_i are the velocity, mass, angular velocity, and moment of inertia of the particle i. $\boldsymbol{f}_{pf,i}$ is the two-phase interaction force. $\boldsymbol{f}_{c,ij}$ is the collision force between particles or particles and wall. A soft-sphere approach with the spring–slider–dashpot model is used for the collision force calculation [11,32] and is summarized in Table 1. k_c is the number collision contacts for the particle i. $\boldsymbol{M}_{ij}$ is the torque due to the collision of particle/particle or particle/wall. The Brownian motion of particles is not considered due to the relatively large particle size ($d \gg 1$ μm). In the present system, the drag force $\boldsymbol{f}_d$ depends on particle volume fraction and the relative velocity difference between the particles and fluid, as follows [33]

$$\boldsymbol{f}_{\mathrm{d}} = \frac{\pi}{8} C_{\mathrm{d}} \rho_f d^2 \alpha_f^{2-\chi} \left|\boldsymbol{u}_r\right| \boldsymbol{u}_r \,, \tag{7}$$

$$C_{\mathrm{d}} = \left(0.63 + \frac{4.8}{\sqrt{Re}}\right)^2 \,, \tag{8}$$

$$\chi = 3.7 - 0.65\exp\left(-\frac{(1.5 - \log Re)^2}{2}\right) \,, \tag{9}$$

$$Re = \frac{\left|\boldsymbol{u}_r\right| d}{\nu_f} \,, \tag{10}$$

where C_d denotes the drag coefficient, which is a function of the particle Reynolds number Re. χ is an empirical constant. $\boldsymbol{u}_r = \boldsymbol{u} - \boldsymbol{v}$ is the relative velocity difference between the particles and fluid. The pressure gradient force is written as $\boldsymbol{f}_{\nabla p} = -V_p \nabla p$, where V_p is the particle volume. The virtual mass force is expressed as $\boldsymbol{f}_{vm} = -0.5\rho_f V_p \left(\mathrm{D}\boldsymbol{u}/\mathrm{D}t - \mathrm{d}\boldsymbol{v}/\mathrm{d}t\right)$.

Table 1
Expressions of collision forces.

Expressions	Variables
$\boldsymbol{f}_{c,ij} = \boldsymbol{f}_{n,ij} + \boldsymbol{f}_{t,ij}$	Collision force
$\boldsymbol{f}_{n,ij} = k_n \boldsymbol{\delta}_n - \eta_n \Delta \mathbf{U}_n$	Normal collision force
$\boldsymbol{f}_{t,ij} = \begin{cases} k_t \boldsymbol{\delta}_t - \eta_t \Delta \mathbf{U}_t & \left\|\boldsymbol{f}_{t,ij}\right\| \le -\mu_s \left\|\boldsymbol{f}_{n,ij}\right\| \frac{\Delta \mathbf{U}}{\left\|\Delta \mathbf{U}\right\|} \\ -\mu_s \left\|\boldsymbol{f}_{n,ij}\right\| \frac{\Delta \mathbf{U}}{\left\|\Delta \mathbf{U}\right\|} & \left\|\boldsymbol{f}_{t,ij}\right\| > -\mu_s \left\|\boldsymbol{f}_{n,ij}\right\| \frac{\Delta \mathbf{U}}{\left\|\Delta \mathbf{U}\right\|} \end{cases}$	Tangential collision force
$k_n = \frac{4}{3} Y^* \sqrt{R^* \left\|\boldsymbol{\delta}_n\right\|}$	Normal spring constant
$\eta_n = 2\sqrt{\frac{5}{6}} \beta \sqrt{S_n m^*}$	Normal damping coefficient
$k_t = 8 G^* \sqrt{R^* \left\|\boldsymbol{\delta}_n\right\|}$	Tangential spring constant
$\eta_t = 2\sqrt{\frac{5}{6}} \beta \sqrt{S_t m^*}$	Tangential damping coefficient

where
$\frac{1}{Y^*} = \frac{\left(1-\nu_i^2\right)}{Y_i} + \frac{\left(1-\nu_j^2\right)}{Y_j}$, $\frac{1}{R^*} = \frac{1}{R_i} + \frac{1}{R_j}$, $\frac{1}{m^*} = \frac{1}{m_i} + \frac{1}{m_j}$, $\beta = \frac{ln(e)}{\sqrt{ln^2(e)+\pi^2}}$
$\frac{1}{G^*} = \frac{2(2+\nu_i)(1-\nu_i)}{Y_i} + \frac{2(2+\nu_j)(1-\nu_j)}{Y_j}$, $S_n = 2Y^* \sqrt{R^* \left\|\boldsymbol{\delta}_n\right\|}$, $S_t = 8G^* \sqrt{R^* \left\|\boldsymbol{\delta}_t\right\|}$,
μ_s is the sliding friction coefficient, Y is the Young's modulus,
G is the shear modulus, ν is the Poisson ratio,
and e is the coefficient of restitution.

2.2. Interphase coupling

In the CFD-DEM simulation, the interactions between the fluid and particles are coupled based on the void fraction and the momentum exchange. The CFD cells and particles are linked with each other through the particle locations [34]. Firstly, proper functions need to be given to distribute the particle quantities in CFD equations because a Dirac delta shaped function may cause numerical errors [35]. Secondly, the fluid phase properties at the CFD cell centers or face centers need to be interpolated to the particle positions for updating the particle motions. In this paper, the diffusion based method [7,36] is used to map the particle quantities (particle volume fraction, particle velocity, drag force, and etc.) to the CFD mesh because the particle sizes are comparable to or larger than the computational cell sizes. A transient, homogeneous diffusion equation is solved in the computational domain that is initiated with these particle quantities to obtain smooth fields. A Neumann boundary condition with no-flux (zero gradient) is specified at all physical boundaries to ensure the conservation of the particle quantities.

For coarse particles, whose size is comparable to the computational cell size, one must be able to account for the fluid flow information on a larger scale than that of a single cell for accurately estimating the two-phase interactions [34,37]. A possible procedure is interpolating the fluid flow information from the surrounding CFD cells of the particle to the particle position. In this paper, we develop a volume averaged

method for estimating the background fluid velocity and particle volume fraction from the surrounding cells. The particle is expanded by five times to obtain the neighboring cell labels. The cells whose center point is within the expanded particle boundary are defined as the neighboring cells. Then, the background fluid velocity is calculated as follows

$$\boldsymbol{u}(\boldsymbol{x}) = \frac{\sum_{j=1}^{N} \boldsymbol{u}(\boldsymbol{x}_j) V_{c,j}}{\sum_{j=1}^{N} V_{c,j}}, \tag{11}$$

where $\boldsymbol{u}(\boldsymbol{x})$ is the background fluid velocity at the particle position. $\boldsymbol{u}(\boldsymbol{x}_j)$ and $V_{c,j}$ are the fluid velocity and cell volume of the cell j. N is the number of cells in the expanded region. The corrected relative velocity difference $\boldsymbol{u}_r$ in Eq. (7) is written as

$$\bar{\boldsymbol{u}}_r(\boldsymbol{x}) = \frac{\sum_{j=1}^{N_c} \boldsymbol{u}(\boldsymbol{x}_j) V_{c,j}}{\sum_{j=1}^{N_c} V_{c,j}} - \boldsymbol{v}. \tag{12}$$

Similarly, the corrected particle volume fraction for drag force calculation is expressed as

$$\bar{\alpha}_p(\boldsymbol{x}) = \frac{\sum_{j=1}^{N_c} \alpha_p(\boldsymbol{x}_j) V_{c,j}}{\sum_{j=1}^{N_c} V_{c,j}}, \tag{13}$$

where $\alpha_p(\boldsymbol{x}_j)$ denotes the particle volume fraction in cell j ($\alpha_p(\boldsymbol{x}_j) + \alpha_f(\boldsymbol{x}_j) = 1$). The corrected relative velocity difference and the particle volume fraction are only used for computing the two-phase interaction force while the void fraction and the fluid velocity in Eqs. (1) and (2) use the local value without any correction.

2.3. Numerical configurations

The geometry of the computational domain is shown in Fig. 1. The diameter D and height H of the pipe are 0.05 m and $40D$, respectively. The flow direction is the $+z$ direction. The bottom and top face are set as periodic boundary. The side face is set as a no-slip wall boundary. The angle between the acceleration of gravity and the x direction is β, indicating that the pipe is inclined at an angle of β. In the fluid momentum conservation equation, we add a driving force to assure an expected averaged bulk fluid velocity u_b at each time step. The mesh resolutions are $20 \times 20 \times 1000$ in the x, y, and z directions. Initially, the particles are uniformly distributed in the full of pipe. The numbers of particles N_p are calculated based on the average particle volume fraction as $N_p = 3D^2 H \alpha_p / (2d^3)$. The overall particle volume fraction remains constant during the simulation due to the periodic boundary condition. Facilitated with the above initial and boundary conditions, the governing equations in Section 2.1 are solved in the open-source code CFDEM [38], which couples the open-source code OpenFOAM and LIGGGHTS [39]. The CFD governing equations are discretized using second-order central difference scheme for the pressure gradient and divergence terms. The advection term is discretized based on the second-order Gauss linear scheme. The second-order backward scheme is used for temporal discretization. The pressure-implicit with splitting of operators (PISO) algorithm [40] is chosen to couple the velocity and pressure. The time steps are chosen in order to keep the DEM time step less than 10% the Rayleigh time [41,42]

$$t_R = \frac{0.5\pi d}{0.163\nu + 0.8766} \sqrt{\frac{2\rho_p (1+\nu)}{Y}}, \tag{14}$$

where ρ_p is the particle density. The Rayleigh time is 9.6×10^{-5} s in this work. Hence, the DEM time step is set as 1×10^{-5} s. In addition, Tsuji et al. [43] proposed that the CFD time step should be 10–100 times larger than the DEM time step. As a result, the CFD time step is set as 5×10^{-4} s.

The controlling dimensionless parameters that characterize the dense particulate flows in inclined pipe containing the Reynolds number of the flow, $Re_f = \rho_f u_b D / \mu_f$, the particle volume fraction, α_p, the pipe inclination angle, β, the density ratio, $s = \rho_p / \rho_f$, the Stokes number, $St = \rho_p d^2 u_b / (18 \mu_f D)$, and the Froude number, $Fr = u_b / \sqrt{gD}$ [44,45]. For the two-phase flows in inclined pipe, gravity can play an important role in the flow behavior. Hence, the Froude number is included, which indicates the ratio of the flow inertia to the gravity effect. The Stokes numbers $St = 8.9$, 20 and 35.6 are varied by changing the particle diameter for fixed particle density $\rho_p = 2000$ kg/m^3, fluid average bulk velocity $u_b = 1$ m/s, and fluid viscosity $\mu_f = 0.001$ Pa s to make the Reynolds number of the flow Re_f unchanged. The particle volume fraction is set as 0.05, 0.10, 0.15, and 0.20. The pipe inclination angle is set as 10°, 30°, 45°, 60°, and 75°. Furthermore, the Froude number based on the given fluid average bulk velocity $u_b = 1$ m/s and pipe diameter $D = 0.05$ m is 1.4 under terrestrial gravitational acceleration $g = 9.81$ m/s^2. To investigate the effect of the Froude numbers on the flow characteristics in inclined pipe, five values are employed, $Fr = 5.7$, 11.4, 22.8, 25 and 30. The variation of the Froude number is achieved by varying the gravitational acceleration g to retain the same Stokes number.

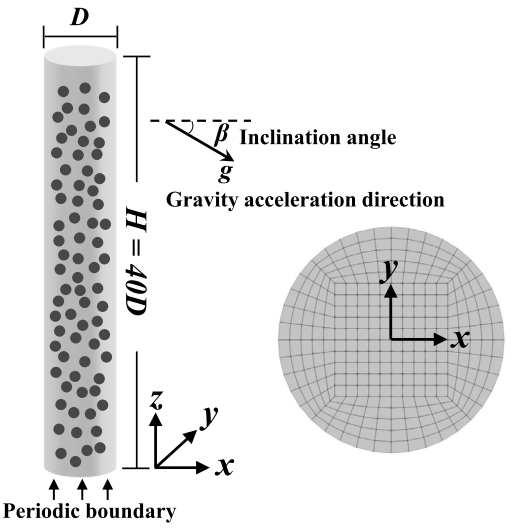

Fig. 1. Schematic representation of three-dimensional computational domain. The particles are uniformly distributed in the domain initially.

2.4. Model validation

To verify the reasonability of the numerical model in this paper for simulating the dense particulate flows in pipe, two test cases are taken. The first one is a fluidized bed validation case, which references the experiment of Müller et al. [46,47]. The geometry of the computation domain is a cuboid with size of 10 mm × 44 mm × 120 mm in x, y, and z directions. The density and diameter of the particles are 1000 kg/m^3 and 1.2 mm, respectively. The fluid density is 1.2 kg/m^3 and viscosity is 1.5×10^{-5} m^2/s. Initially, particles are freely packed at the bottom of the column to form a particle bed with height of 30 mm. Thereafter, a flux of fluid is introduced from the bottom to fluidize the particle bed. Müller et al. [46,47] used magnetic resonance to measure the time-averaged fluid volume fraction and the particle velocity. Therefore, the simulation results can be compared to the experimental measurement. The mesh resolutions are $8 \times 36 \times 100$ in x, y, and z directions. The pressure boundary condition on the upper z and lower z face is set as a fixed value and zero gradient, respectively. The fluid velocity is set as zero gradient on the upper z face and fixed value of $u_z = 0.9$ m/s on the lower z face. At the four side faces, the fluid velocity is set as zero value and the pressure is set as zero gradient. The time-averaged fluid volume fraction at the height of $z = 16.4$ mm and particle vertical velocity at the height of $z = 15$ mm are extracted

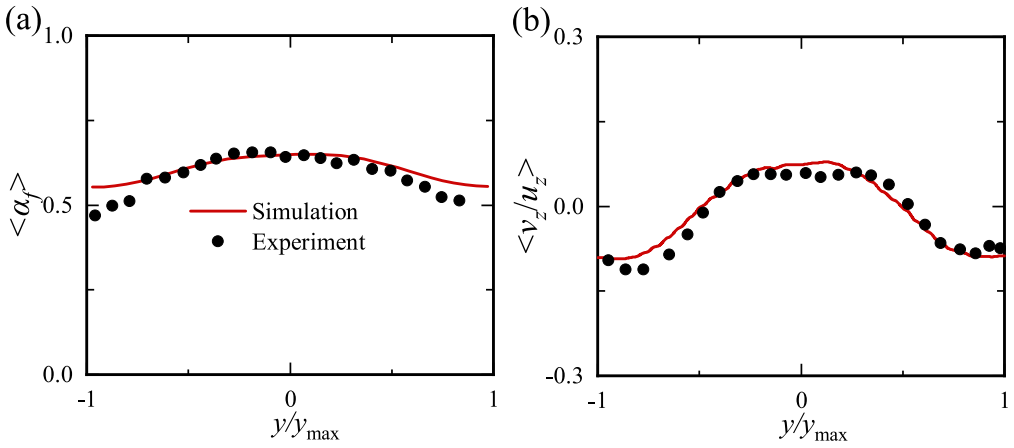

Fig. 2. The time-averaged results obtained from numerical simulation with (a) fluid volume fraction at the height of z = 16.4 mm, and (b) particle vertical velocity at the height of z = 15 mm. The experimental measurement data are also given for comparison.

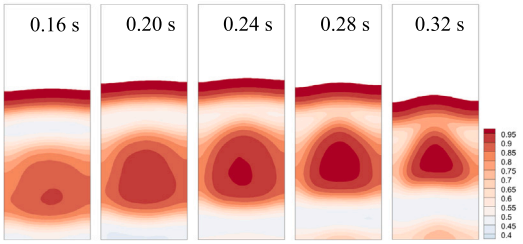

Fig. 3. The contour of fluid volume fraction at different times, 0.16 s, 0.20 s, 0.24 s, 0.28 s, and 0.32 s.

from the numerical simulation because the experimental measurement data are on these two sections. The average time is 20 s, which is long enough to obtain statistically time-averaged results. Fig. 2 gives the time-averaged fluid volume fraction and particle vertical velocity. The particle vertical velocity v_z is normalized by the fluid inlet velocity u_z. The average values of numerical simulation results agree well with the experimental measurement data. To show the flow regimes of the fluidized bed, we give the contour of fluid volume fraction at different times in Fig. 3. The bubble formation (0.16 s), growth (0.24 s) and burst (0.32 s) can be clearly identified. The bubble dynamics observed in the numerical simulation are physically reasonable as confirmed in previous experiments [46,47].

The second test case in a sediment transport process at the boundary layer in a channel. The size of the channel is $60d\times 120d\times 40d$ in x, y, and z directions, respectively, where d is the particle diameter. The particle diameter is 1 mm in this case. The flow is in the $+y$ direction, and the gravity acceleration is in the $-z$ direction. The four faces in the y and x directions are set as periodic. The bottom z face is set as a no-slip boundary and the top z face is set as a free-slip boundary. A driving force is added in the fluid momentum conservation equation to assure an expected averaged bulk fluid velocity u_b. The cell numbers in the three directions (x, y, and z) are 60, 120, and 40, respectively. The density and viscosity of the fluid phase are 1000 kg/m^3 and 0.001 Pa s. The density of the particles is 2650 kg/m^3. The average bulk fluid velocity varies from 0.1 m/s to 1.0 m/s. All the parameters used in the simulation are given in Table 2. Each simulation case is performed for 50 flow-through times for time averaging. Similar to the monodisperse fluid-solid fluidized bed above, the particles are freely packed at the bottom initially. Then the average bulk fluid velocity is set as a constant value. When the average bulk fluid velocity is small, particles on the bed surface start creeping under the shear stress and the fluid drag force. This process is called bed-load regime. When the average bulk fluid velocity is large enough, more particles are suspended in the fluid region above the particle bed. This process is called suspended-load regime. The particle velocities in y direction and distribution under the average bulk fluid velocities of 0.2 m/s and 1.0 m/s are shown in Fig. 4a and b. The particle velocities are non-dimensionalized by the average bulk fluid velocity. It can be seen in the figure that the particle regime is bed-load dominated with the average bulk fluid velocity of 0.2 m/s and suspended-load dominated with the average bulk fluid velocity of 1.0 m/s. In the sediment transport process, the time-averaged, vertically integrated, volumetric sediment flux q_{sy} is positively correlated with shear velocity u_*. The u_* can be calculated from the time-averaged two-phase interaction force as $u_* = \sqrt{H\left\langle \boldsymbol{F}_{pf}\right\rangle/\rho_f}$, where H is the channel height and $\langle\rangle$ is the time average operator. The non-dimensional sediment fluxes q^* and the non-dimensional shear stress τ^* (Shields parameter) are calculated as

$$q^* = \frac{q_{sy}}{\sqrt{(s-1)gd^3}} = \frac{\sum_i V_{p,i}v_{y,i}}{A\sqrt{(s-1)gd^3}}, \tag{15}$$

$$\tau^* = \frac{\rho_f u_*^2}{(\rho_p-\rho_f)gd}, \tag{16}$$

where $V_{p,i}$ is the volume of particle i, and $v_{y,i}$ is the velocity of particle i in y direction, and A is the horizontal plane area. The relationship between the nondimensional sediment fluxes q^* and Shields parameter τ^* is given in Fig. 4c. The empirical curve proposed by Wong and Parker [48] and Nielsen [49], the simulation results of the method of Sun and Xiao [50], the experiment results of Schmeeckle [51] are also given for comparison. The simulation results also agree well with the experimental results and the results in previous studies. As a result, the numerical model in this paper is used for investigating the dense particulate flows in inclined pipe.

2.5. Change of Froude number

There are two ways to obtain various Froude number Fr with the Reynolds number of the flow Re_f, the density ratio s, particle volume fraction α_p, the pipe inclination angle β, and the Stokes number St unchanging. The first way is only changing the value of gravitational acceleration g, which is very simple in the numerical simulation. The second way is to change the average fluid bulk velocity and the pipe diameter together with constant gravitational acceleration $g = 9.81$ m/s^2. In order to prove that the two ways have the same effect, we set different simulation cases for comparison (as shown in Table 3). The Stokes number St, the density ratio s, the particle volume fraction α_p, pipe inclination angle β and the Reynolds number of the flow Re_f are set as 20, 2.0, 0.1, 45° and 50 000, respectively. Fig. 5 shows the

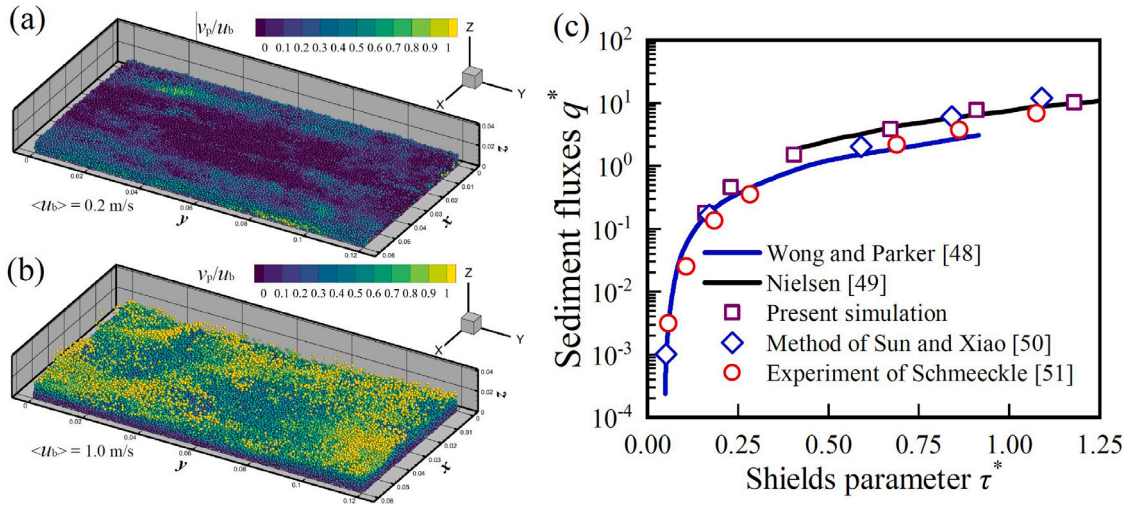

Fig. 4. Simulation results of the sediment transport process at the boundary layer in a channel. The colormaps in subfigures (a) and (b) represents the ratio of particle velocity in the y direction to the fluid bulk velocity u_b. u_b in (a) and (b) is 0.2 m/s and 1.0 m/s, respectively. Subfigure (c) is nondimensional sediment fluxes versus Shields parameters. The blue solid line represents the empirical curve proposed by Wong and Parker [48] to describe bed-load regime. The black solid line represents the empirical curve describing suspended-load regime from Nielsen [49]. The red circle and blue diamond are the results in previous studies [50,51].

Table 2
All parameters used in the sediment transport process.

Parameters	Values
Geometry of the channel	
Length, Width, Height	60 mm, 120 mm, 40 mm
Particle properties	
Density	2650 kg/m^3
Diameter	1 mm
Number	87 000
Young's modulus	1.0×10^8 Pa
Poisson's ratio	0.23
Coefficient of restitution	0.10
Sliding friction coefficient	0.10
Fluid properties	
Density	1000 kg/m^3
Viscosity	1.0×10^{-3} Pa s
Bulk average velocity	0.1–1.0 m/s

Table 3
Parameters of the simulation cases to obtain different Froude numbers, Fr, with constant $St = 20$, $\alpha_p = 0.1$, $\beta = 45°$ and $Re_f = 50\,000$.

	Case1	Case2
$Fr = 5.7$	$g = 0.61$ m/s^2 $u_b = 1.0$ m/s $d = 0.003$ m $D = 0.05$ m	$g = 9.81$ m/s^2 $u_b = 2.52$ m/s $d = 0.0012$ m $D = 0.0198$ m
$Fr = 22.8$	$g = 0.038$ m/s^2 $u_b = 1.0$ m/s $d = 0.003$ m $D = 0.05$ m	$g = 9.81$ m/s^2 $u_b = 6.307$ m/s $d = 0.00047$ m $D = 0.0078$ m

comparisons of the time-averaged particle velocity $\langle v_z \rangle$ (in z direction), fluid velocity $\langle u_z \rangle$ (in z direction) and particle volume fraction $\langle \alpha_p \rangle$ at the middle of the pipe ($z = 20D$). The time-averaged particle velocity and fluid velocity are non-dimensionalized by the average fluid bulk velocity. It can be seen in the figure that the particle velocity, the fluid velocity and the particle volume fraction collapse well for both Case 1 and 2, for the two Froude numbers, $Fr = 5.7$ and $Fr = 22.8$. That is, the Froude number represents the gravity effect despite significant differences in the absolute values of the gravitational acceleration g, the particle diameter d, the pipe diameter D, and the average fluid bulk velocity u_b. The comparison confirms the equivalence between the two ways for obtaining different Froude numbers. Due to the change of gravitational acceleration g in the numerical simulation is very simple, the subsequent sections of this paper use the first way (Case 1) to vary Fr. From Fig. 5, it can also be seen that the particle velocity and volume fraction show two distinct distributions, asymmetric and approximately symmetric. When the Froude number is larger, i.e. a decrease in g or alternatively, where an decrease in the size of D, the particle velocity and volume fraction are closer to a symmetrical distribution. This is because the gravitational effect is reduced and more particles are in suspension in the inclined pipe, which is similar to the suspended-load regime in sediment transport process.

3. Results and discussion

3.1. Two flow regimes

Based on the validated CFD-DEM model, different flow regimes and the resulting flow characteristics are investigated at different controlling dimensionless parameters. Fig. 6 presents two different flow regimes that can be generated, depending on the combination of values of the Stokes number St, and the Froude number Fr ($\beta = 45°$, $\alpha_p = 0.1$): (1) The first one is termed a gravity-dominant regime, which occurs the particle volume fraction is sufficiently high to lead to significant flow resistance in the lower region of the inclined pipe under a significant influence of gravity (e.g., $St = 20$, $Fr = 5.7$); and (2) The second one is termed a particle-inertia-dominant regime, which occurs for relatively weak gravitational effect (e.g., $St = 20$, $Fr = 22.8$). The non-dimensionalized particle velocity $\langle v_z/u_b \rangle$, fluid velocity $\langle u_z/u_b \rangle$ and the particle volume fraction $\langle \alpha_p \rangle$ are all shown for the two regimes. In addition, we also give the particle distribution on the pipe cross-section with $z = 20D$ at time of 15 s. The particles are colored by particle velocities in z direction to show various particle behaviors better.

For the gravity-dominant regime, the profiles of $\langle v_z/u_b \rangle$, $\langle u_z/u_b \rangle$, and $\langle \alpha_p \rangle$ are asymmetric about the cross-sectional pipe plane. Both the particle and fluid velocities are larger in the upper half of the pipe than that in the lower part. All the particles settle down to the bottom of the inclined pipe and form a thick particle bed. The particles move upward in the form of a moving bed, where only a few particles are suspended in the upper fluid region. In the lower region of the pipe, the particle velocity ($\langle v_z/u_b \rangle$) gradually increases with the distance from the bottom

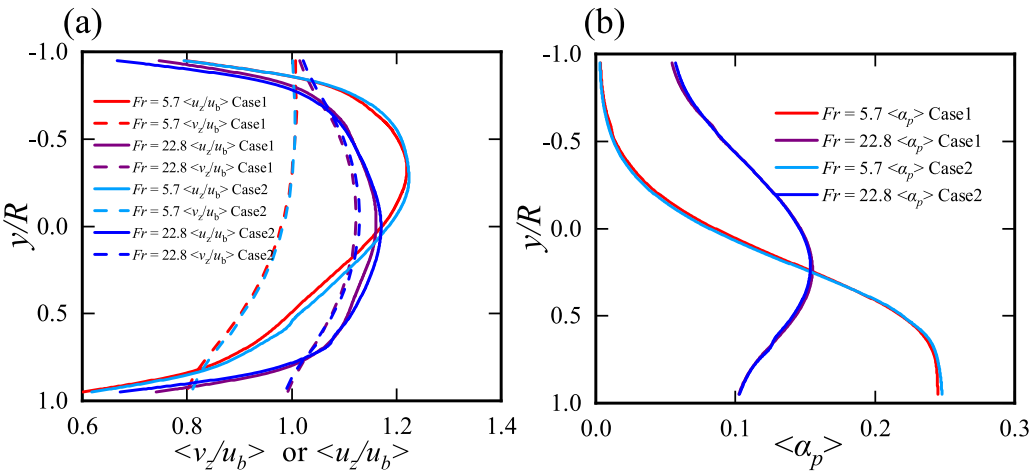

Fig. 5. Comparisons of the (a) time-averaged particle velocity $\langle v_z/u_b \rangle$ (in z direction), fluid velocity $\langle u_z/u_b \rangle$ (in z direction) and (b) particle volume fraction $\langle \alpha_p \rangle$ at the middle of the pipe with the two cases shown in Table 3. Here the brackets $\langle\rangle$ indicate the time average operator. The y-axis represents the radial distance normalized by the pipe radius, where $y/R = 1.0$ and -1.0 refer to the bottom and top of the pipe wall, respectively. The particle volume fraction is 0.1 and the pipe inclination angle is 45°.

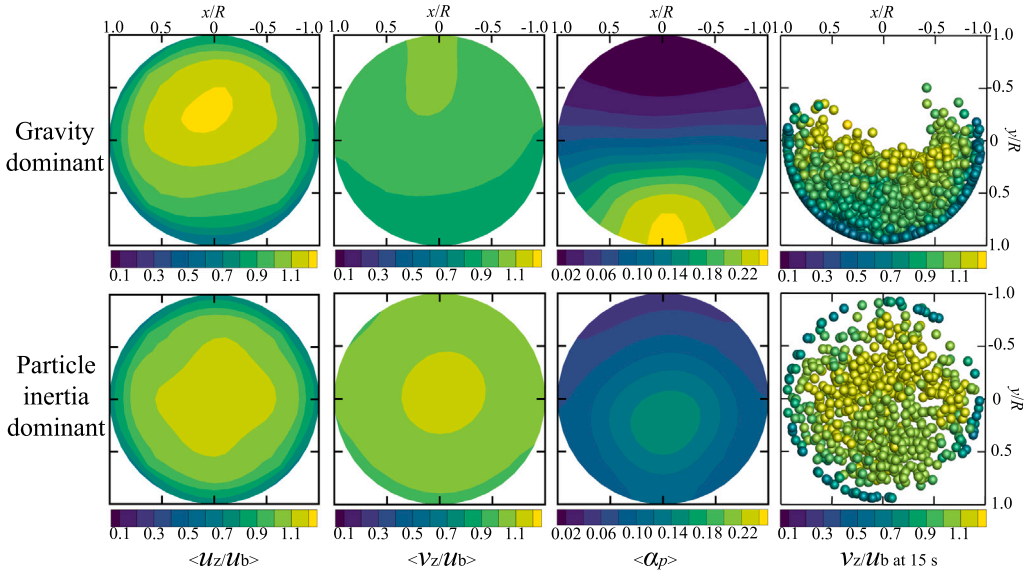

Fig. 6. Non-dimensionalized particle velocity $\langle v_z/u_b \rangle$, fluid velocity $\langle u_z/u_b \rangle$ and the particle volume fraction $\langle \alpha_p \rangle$ in the two flow regimes: gravity-dominant regime ($St = 20$ and $Fr = 5.7$) and particle-inertia-dominant regime ($St = 20$ and $Fr = 22.8$). The particle distribution colored by the particle instantaneous velocity on the pipe cross-section plane with $z = 20D$ and time of 15 s is also given to illustrate the flow regime. The particle volume fraction is 0.1 and the pipe inclination angle is 45°.

of the pipe, increasing approximately from 0.8 to 1.0 due to the small value of the fluid velocity, which lead to small fluid drag force. The high particle volume fraction in the lower part of the pipe also results in high frequency of collisions between particles and particles and wall to generate a significant loss of the particle momentum and decreases the particle mean velocity.

For the particle-inertia-dominant regime, approximately symmetric distributions can be seen in all the results presented ($\langle v_z/u_b \rangle$, $\langle u_z/u_b \rangle$ and $\langle \alpha_p \rangle$), which results from the dominance of the axial momentum (z direction) over gravity effect. Most of the particles get suspended and thus become full pipe distributed in the radial direction (x or y direction). The particle velocities, fluid velocities as well as the particle volume fraction in the middle part of the pipe are larger than that in the bottom and top part. Compared with the gravity-dominant regime, the velocity slip between the particles and fluid is very small, which shows better followability of the particles. The particle volume fraction also shows different distribution in the two regimes. The particle bed is rather dense especially near the bottom of the pipe in the gravity-dominant regime, having a maximum particle volume fraction larger than 0.25. However, in the particle-inertia-dominant regime, the particle volume fraction become much looser. The maximum value is approximately 0.15.

3.2. Effect of dimensionless number

To illustrate the effect of the dimensionless numbers (Fr, St, β, and α_p) on the flow characteristics in the inclined pipe, Fig. 7 presents the non-dimensionalized values of the time-averaged fluid and particle velocities in the line $z = 20D$ and $x = 0$ for a series of values of St and Fr where $\beta = 45°$ and $\alpha_p = 0.1$. The black solid line represents the fluid velocity and the red solid line denotes the particle velocity. It can be seen in the figure that the velocity slip between the fluid and particles increases with an increase in the value of St. This correlation between $\langle v_z/u_b \rangle$ and St is consistent with the simulation results of Zhang et al. [45] and the experimental measurements of Lau and Nathan [52]. For large Stokes number, which represents the ratio of particle inertia to fluid inertia, the particles have greater inertia and require more

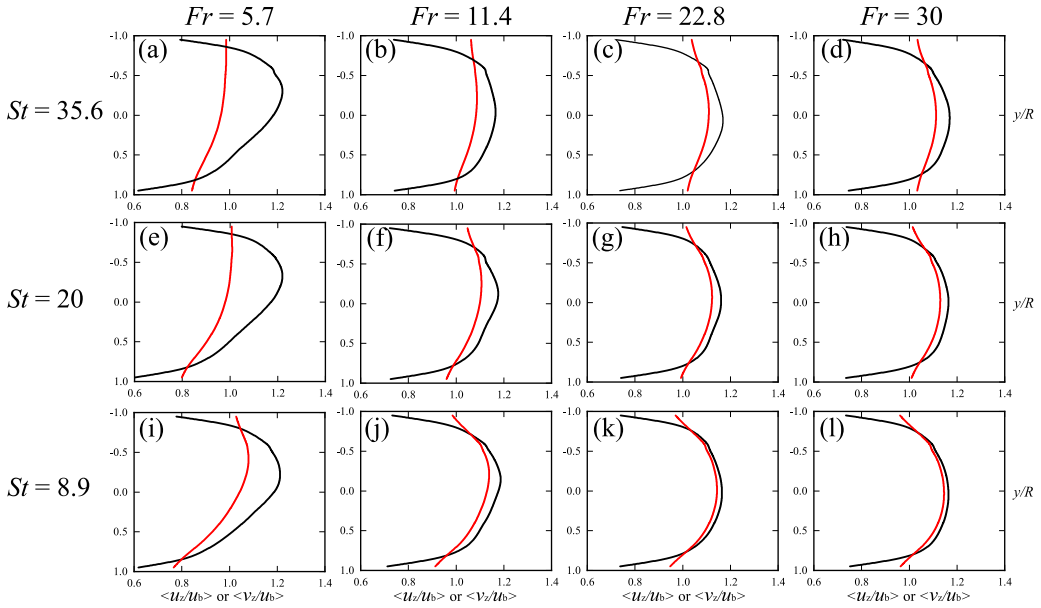

Fig. 7. Non-dimensionalized values of the time-averaged fluid and particle velocities ($\langle u_z/u_b \rangle$ and $\langle v_z/u_b \rangle$) in the line $z = 20D$ and $x = 0$ for a series of values of St and Fr, where the black solid line represents the fluid velocity and the red solid line denotes the particle velocity ($\beta = 45°$ and $\alpha_p = 0.1$).

momentum transfer from the fluid phase because the driving force of the particles motion mainly comes from the drag of the fluid. The particles with larger inertia also have a greater response time. The two factors above lead to larger velocity slip between the particles and fluid. In addition, it can be seen in the figure that St has little impact on the fluid velocity distribution. This is because the particle inertia is larger than the flow inertia (for $8.9 < St < 35.6$), the velocity distribution of the fluid is then determined by the particle volume fraction distribution. In a flow dominated by particle inertia, particle volume fraction distribution is less affected by flow inertia. Hence, the fluid velocity distribution is generally the same under different St.

With an increase in the Froude number Fr, both the fluid and particle velocities show symmetry along the cross section. For example, when the value of Fr is 5.7, the influence of gravitational force on the two-phase velocities is stronger than that for larger Fr. The particle and fluid velocities are larger in the upper part of the inclined pipe than that in the lower part due to most of the particles settle down to the pipe bottom. When the value of $Fr = 30$, the gravitational force has less effect on the flow characteristics than the cases with lower Fr. Most of the particles are in suspension and follow the fluid motion. The particle velocity profile is similar to the fluid velocity and shows symmetry distribution. It is found that when the Froude number is larger than 22.8, both the Stokes number St and Froude number Fr have little impact on the particle velocity distribution (Fig. 7c, d, g, h, k, and l). The particle velocity shows symmetry distribution for $Fr > 22.8$. It means the flow inertia needs to be an order of magnitude higher (approximately 22 times) than gravity effect in the dense particulate flows in an inclined pipe (inclination 45°) before the particle velocity profiles being symmetrical. Hence, it is postulated that particle-inertia-dominant regime could occur where the Froude number is very high. An interesting thing is that for gravity-dominant regime (Fig. 7a,e, and i), the upper part of the particle velocity profiles shows different shape: straight line shape for large St and parabola for small St. This is also because more momentum is required for large inertia particles, which lead to large velocity slip. For the fluid velocity profiles, its shape changes from the heart-shape to the umbrella shape and to the semicircle with an increase in the Fr from 5.7 to 30.

As mentioned above, the fluid velocity distribution is determined by the particle volume fraction distribution, Fig. 8 gives the time-averaged particle volume fraction in the line $z = 20D$ and $x = 0$ for a series of values of St and Fr where $\beta = 45°$ and $\alpha_p = 0.1$. It can be seen that gravity has a strong influence on the local particle volume fraction. When the Froude number is small ($Fr = 5.7$), most of the particles occurs in the bottom of the pipe due to the impact of gravity. The maximum value of the local particle volume fraction is about 2.8 times the initial average particle volume fraction, which is set as 0.1. The local particle volume fraction approaches zero in the upper part of the pipe. In contrast, when the Froude number is larger ($Fr = 30$), the high particle volume fraction distribution shifts towards the pipe axis instead of pipe bottom in all the simulation cases owing to a relatively weak gravitational effect than the flow inertia. It is also shown in the figure that the particle volume fraction is larger in the middle of the pipe than that in the bottom and top for larger Froude number $Fr > 22.8$. However, compared with small values of Fr, the particle volume fraction distribution along the radial direction of the pipe is more uniform, and the maximum value is about 1.3 times the initial average particle volume fraction. In addition, the particle volume fraction profiles change little with the increase of Fr from 22.8 to 30, which means the gravity effects are almost negligible in this region. For small Froude number ($Fr = 5.7$), with an increase in the Stokes number, the maximum value of the particle volume fraction at the pipe bottom decreases approximately from 0.28 to 0.22. The height of the particle bed slightly increases. The particles require more momentum from the fluid phase with larger Stokes number St, which makes more particles suspend above the particle bed and increases the height of particle bed. From Fig. 8, the transition from the gravity-dominant regime to particle-inertia-dominant regime can easily be recognized. In general, compared with the Stokes number, Froude number plays an important role in the regime transition.

Fig. 9 presents the non-dimensionalized values of the time-averaged fluid and particle velocities, and particle volume fraction in the line $z = 20D$ and $x = 0$ for a series of values of initial particle volume fraction (0.05, 0.10, 0.15, and 0.20) with $Fr = 5.7$, $St = 35.6$, and $\beta = 45°$. More particles settle to the pipe bottom for larger particle volume fraction, as shown in Fig. 9b. As a result, the particle resistance on the fluid increases, which leads to the decrease of the fluid velocity at the pipe bottom (Fig. 9a). Because a driving force is added in the fluid momentum conservation equation to assure an expected averaged bulk fluid velocity u_b at each time step, the fluid velocity in the upper

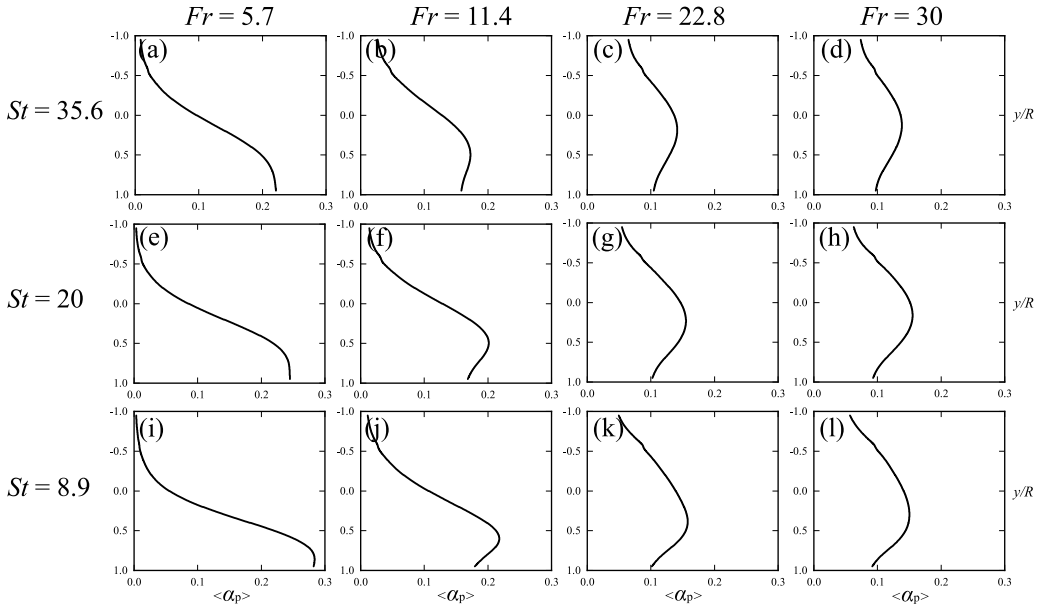

Fig. 8. Time-averaged particle volume fraction $\langle \alpha_p \rangle$ in the line $z = 20D$ and $x = 0$ for a series of values of St and Fr ($\beta = 45°$ and $\alpha_p = 0.1$).

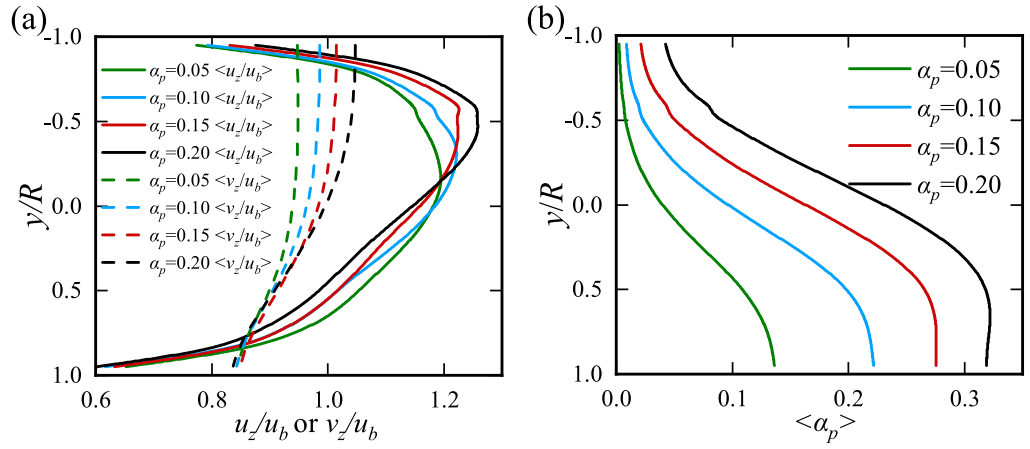

Fig. 9. Non-dimensionalized values of time-averaged (a) fluid and particle velocities ($\langle u_z/u_b \rangle$ and $\langle v_z/u_b \rangle$), (b) particle volume fraction ($\langle \alpha_p \rangle$) in the line $z = 20D$ and $x = 0$ for a series of values initial particle volume fraction α_p. $Fr = 5.7$, $St = 35.6$, and $\beta = 45°$.

part of the pipe increases. The particle volume fraction has little effect on the flow regimes. This may be because the particle volume fraction in this paper is in the dense phase range.

To recognize the transition between the gravity-dominant regime and the particle-inertia-dominant regime, we give the phase diagram of the two regimes under different Stokes numbers St, Froude numbers Fr, and pipe inclination angle β (as shown in Fig. 10). It should be noted that the particle volume fraction is constant, which is set as 0.1. Based on the above discussion, the particles settle to the bottom of the pipe in gravity-dominant regime. The profiles of the particle velocity $\langle v_z/u_b \rangle$ and particle volume fraction $\langle \alpha_p \rangle$ are asymmetric. Especially, the particle volume fraction is very large at the pipe bottom. In contrast, the $\langle v_z/u_b \rangle$ and $\langle \alpha_p \rangle$ are larger in the middle of pipe in particle-inertia-dominant regime. Then, the two regimes are recognized, which is similar to the work of Zhang et al. [45]. The black square dot represents the gravity-dominant regime and the blue triangle denotes the particle-inertia dominant regime. Some regimes cannot be recognized because they are in the transition between the two regimes where both the gravity and particle inertia are important. Therefore, it is marked as transition in Fig. 10 (the red circle in the figure). The region of gravity-dominant regime initially increases and then decreases with the inclination angle increasing from 10° to 75°. The transition area between the two regimes basically presents a linear distribution in the $Fr - St$ diagram. It means the Stokes number and the Froude number all have significant effect on the flow regime in the inclined pipe.

3.3. Temporal variations

The above section mainly focuses on characteristics of the time-averaged value, such as the fluid and particle velocities. In this section, we will analyze the temporal variations of the particle volume fraction and the particle velocity. Fig. 11 demonstrates the temporal variations of the particle volume fraction α_p and particle velocity (in z direction) v_z at the location of $z = 20D$ under different Froude numbers (Fr = 5.7, 11.4, 22.8, and 30) where $\beta = 45°$, $\alpha_p = 0.1$, and $St = 35.6$. With an increase of Fr from 5.7 to 30, the flow regime gradually transits from gravity-dominant regime ($Fr = 5.7$) to particle-inertia-dominant regime (Fr = 22.8 and 30). The time and particle velocity are non-dimensionalized by the particle turnover time $t_p = d/u_b$ and the average bulk fluid velocity u_b. In this figure, the results are averaged

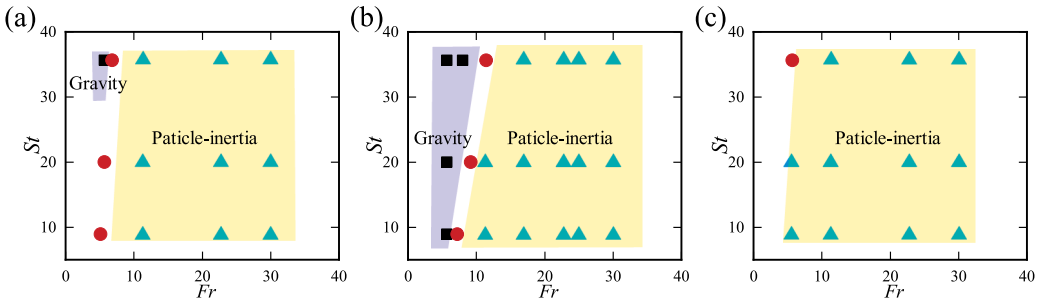

Fig. 10. The flow regimes: gravity-dominant regime and particle-inertia-dominant regime under different Stokes numbers St and Froude numbers Fr. The particle volume fraction α_p is 0.1. The pipe inclination angles β are (a) 10°, (b) 45°, and (c) 75°, respectively. The flow regime recognition is based on the profiles of the particle velocity and particle volume fraction.

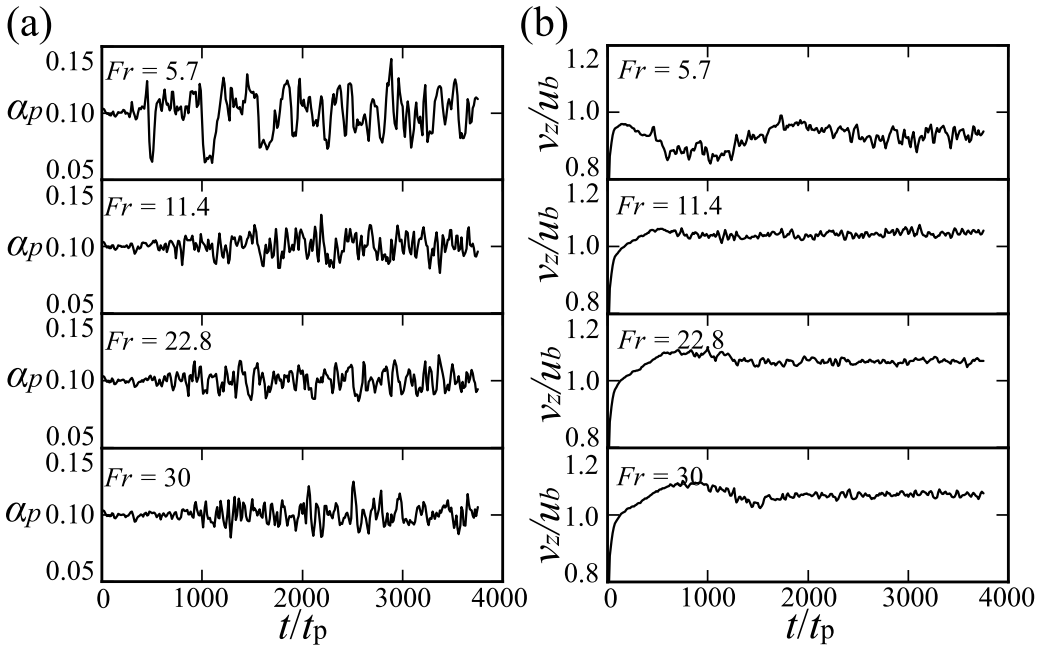

Fig. 11. Temporal variations of (a) the particle volume fraction and (b) particle velocity (in z direction) at the location of $z = 20D$ under different Froude numbers (Fr = 5.7, 11.4, 22.8, and 30). The time and particle velocity are non-dimensionalized by the particle turnover time $t_p = d/u_b$ and the average bulk fluid velocity u_b ($\beta = 45°$, $\alpha_p = 0.1$, and $St = 35.6$).

over the cross-section. Expectedly, when the flow regime is in the gravity-dominant stage, significant fluctuations are observed for both the particle volume fraction and particle velocity. It is attributed to the heterogeneous variable structure of the flow, which results from the frequent particle–particle collisions [7]. For the particle-inertia-dominant regime, most of the particles are suspended in the inclined pipe and the distance of the particles are larger than that in the gravity-dominant regime. Hence, the particle velocity fluctuations decrease due to the reduce of particle collision frequency. However, compared with the particle velocity, the fluctuations of the particle volume fraction also are still evident, which is mainly caused by the density waves or kinematic waves [53,54].

The upward-propagating waves can be observed after the minimum fluidization state in solid–liquid two phase flow in a vertical pipe, as well as in the inclined pipe. In the particle-inertia-dominant regime, the average bulk fluid velocity is far greater than the minimum fluidization velocity. Therefore, the particle volume fraction will exhibit a wave structure that propagates with the same velocity. The fluctuations of the particle volume fraction $\alpha_p' = \alpha_p - \langle \alpha_p \rangle$ over z and t under different Froude numbers are given in Fig. 12a to c. Other dimensionless parameters are $\beta = 45°$, $\alpha_p = 0.1$, and $St = 35.6$. It is found that the noise and superposition of waves with different modes makes the waves difficult to quantify in Fig. 12a to c. Hence, we make a Fourier reconstruction of the fluctuations of the particle volume fraction referring to the work of Willen et al. [54] and Yao et al. [25] with

$$f(z,t) = \sum_{l=-N}^{N} f_l(t) \exp\left(ik_l z\right) , \tag{17}$$

where $f(z,t)$ denotes $\alpha_p'(z,t)$ for easily introducing the reconstruction procedure, $k_l = 2\pi l/H$ is wave number, l is an integer and

$$f_l(t) = \frac{2}{V} \int_0^{z_{max}} \exp(ik_l z) f(z,t) \mathrm{d}z , \tag{18}$$

where V is the volume of the computational domain, and z_{max} is the maximum value of z. The value of N can be estimated by recognizing the smallest features of the fluctuations of particle volume fraction. The shortest wavelength is chosen as two pipe diameters with $N = H/(2D) = 20$. Then the reconstructed particle volume fraction fluctuations are shown in Fig. 12d to f, which clearly shows the wave structure. To calculate the wave velocity, we transform z–t space to the frequency ω and wave number k space as

$$F_1(k,t) = 2 \int_0^{z_{max}} f(z,t) \exp(-ikz) dz , \tag{19}$$

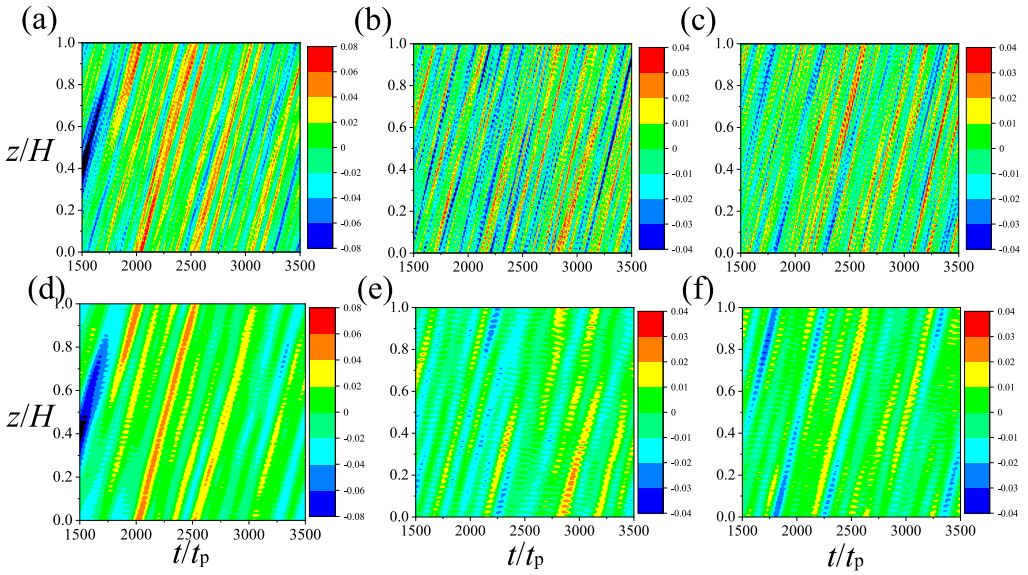

Fig. 12. Fluctuations of the particle volume fraction $\alpha_p' = \alpha_p - \langle \alpha_p \rangle$ with time t/t_p and z coordinate z/H under different Froude numbers: $Fr = 5.7$ in subfigures (a, d), $Fr = 11.4$ in subfigures (b, e), and $Fr = 22.8$ in subfigures (c, f). The subfigures d–f are the Fourier reconstruction of the particle volume fraction fluctuations ($\beta = 45°$, $\alpha_p = 0.1$, and $St = 35.6$).

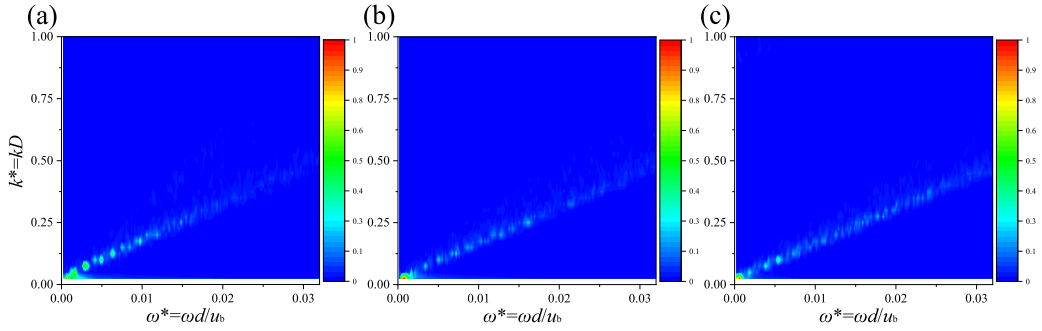

Fig. 13. Power spectra of the fluctuation of the particle volume fraction under different Froude numbers (a) $Fr = 5.7$, (b) $Fr = 11.4$, and (c) $Fr = 22.8$. The wave frequency and wave number are non-dimensionalized as $\omega^* = \omega d/u_b$ and $k^* = kD$. ($\beta = 45°$, $\alpha_p = 0.1$, and $St = 35.6$).

$$F_2(k,\omega) = 2\int_0^{t_{max}} F_1(k,t)\exp(-i\omega t)dt\,, \tag{20}$$

where t_{max} is the maximum value of time. Fig. 13 gives the squares of the Fourier transform coefficients $|F_2(k,\omega)|^2$ as functions of the wave frequency and wave number, which is also called the power spectra of the waves. The spectra are normalized by the maximum value in each case. The wave frequency and wave number are non-dimensionalized as $\omega^* = \omega d/u_b$ and $k^* = kD$. It is shown in the figure that there is a linear relationship between wave number and frequency. Then the wave velocity is calculated as $c = \omega/k$.

Fig. 14 presents the kinematic wave velocity during the particle transportation under different controlling parameters, such as the pipe inclination angle, particle volume fraction, and Stokes number. Except for the changed parameters, the other parameters are $\beta = 45°$, $St = 35.6$. The kinematic wave velocity increases with Fr, β, and α_p increasing. Generally, the wave velocity can be estimated from the particle flux F with $c = \partial F/\partial\alpha_p$ [55]. For high Fr, the flow regime is particle-inertia-dominant regime where most of the particles are in suspension. It makes the particle flux larger in high Fr than that in low Fr. Similarly, when the particle volume fraction is large, the particle flux is also large, lead to large wave velocity. It is worth noting that St has little effect on the kinematic wave velocity, which is consistent with the study of van Wijk et al. [55].

3.4. Flow regime transition

For a better understanding of the particle distribution in different flow regimes, the pair probability distribution function proposed by Yin and Koch [56] is used to measure the microstructure or anisotropy

$$P(\boldsymbol{r}) = \frac{0.25\pi D^2 H}{N_p^2}\left\langle \sum_{i=1}^{N_p}\sum_{j=1,j\neq i}^{N_p}\delta\left(\boldsymbol{r}-\boldsymbol{r}_{ij}\right)\right\rangle, \tag{21}$$

where $\boldsymbol{r}_{ij} = (r_{ij}, \theta_{ij})$ is the vector between particle i and j. In cylindrical polar coordinates, $r_{ij} = \|\boldsymbol{x}_i - \boldsymbol{x}_j\|$, where $\boldsymbol{x}_i$ and $\boldsymbol{x}_j$ are the position vector of the particle i and j, respectively. The θ_{ij} is expressed as

$$\theta_{ij} = \begin{cases} \arccos(|z_i - z_j|/r_{ij}), & z_i - z_j < 0 \\ \arcsin(|z_i - z_j|/r_{ij}), & z_i - z_j \geq 0 \end{cases}. \tag{22}$$

We plot the colormaps of $P(r,\theta)$ under different Fr ($Fr = 5.7$, 11.4, and 30), as shown in Fig. 15. Here θ is the angle relative to the transportation direction or pipe axis direction. The pair probability is symmetric about the pipe axis plane ($\theta = 90°$). The Stokes number is 35.6 and the pipe inclination angle is 45°. The particle volume fraction

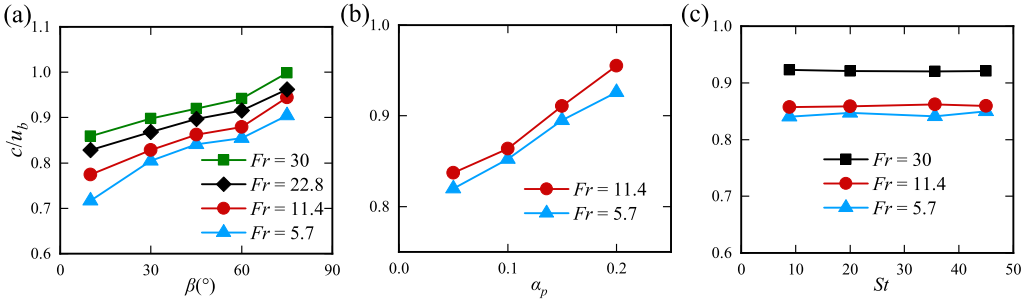

Fig. 14. Non-dimensionalized values of the wave velocity c/u_b for a series of values of St and Fr.

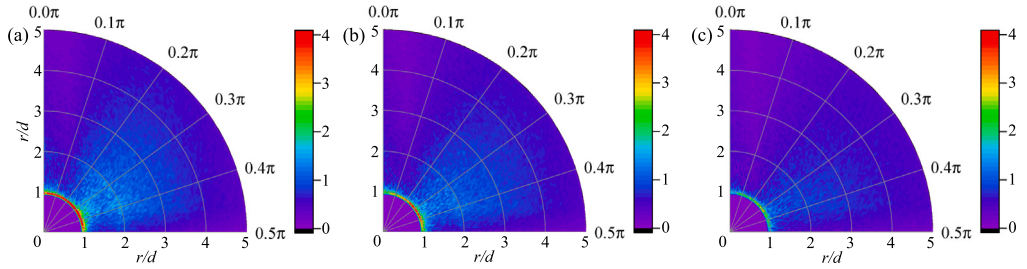

Fig. 15. The pair probability density distribution $P(r,\theta)$ of dense particulate flow in inclined pipe: (a) $Fr = 5.7$, (b) $Fr = 11.4$, and (c) $Fr = 30$. Other parameters are $St = 35.6$, $\alpha_p = 0.1$, and $\beta = 45°$.

is 0.1. For $Fr = 5.7$ and 11.4, a peak in the pair probability can be found in the $\theta = 55$–$90°$ direction. This microstructure suggests that there is a tendency for the particles to settle to the pipe bottom during the transportation. By comparing $P(r,\theta)$ in $Fr = 30$ with that in $Fr = 5.7$ and 11.4, we can immediately see that the microstructure is more anisotropic and inhomogeneous for small Fr. It is due to the fact that most of the particles are in suspension for large Fr.

The regimes of dense particulate flows with coarse particles in inclined pipe are governed by various forces, such as the drag force, the gravity force, and the particle collision force. The analyze of these forces is helpful for investigating the particle dynamics, thereby gaining insights into the flow regimes. Inspired by the work of Zhou et al. [11], we analyze the volumetric particle collision force and the fluid–particle interaction force at the particle scale. Two dimensionless number, the collision stress σ_{col} and the fluid–particle interaction stress σ_{pf}, are defined, which are the ratios of unit particle collision force and unit fluid–particle interaction force to unit particle buoyant force, respectively

$$\sigma_{col} = \frac{\left\langle \frac{1}{N_p}\sum_{n=1}^{N_p} |\boldsymbol{f}_c|_n \right\rangle}{\left\langle \frac{1}{N_p}\sum_{n=1}^{N_p} (\rho_p - \rho_f) V_{pn} g \right\rangle}, \tag{23}$$

$$\sigma_{pf} = \frac{\left\langle \frac{1}{N_p}\sum_{n=1}^{N_p} |\boldsymbol{f}_{pf}|_n \right\rangle}{\left\langle \frac{1}{N_p}\sum_{n=1}^{N_p} (\rho_p - \rho_f) V_{pn} g \right\rangle}, \tag{24}$$

where V_{pn} is the volume of particle n. Fig. 16a demonstrates the relationship between σ_{pf} and σ_{col} under different Fr and St. σ_{pf} increases with the increase of σ_{col}. This trend is similar to the work of Zhou et al. [11] and is attributed to the vigorous particle motion, where the particle–particle and particle–fluid interactions are enhanced. However, we cannot recognize the regime transition in Fig. 16. In the work of Zhou et al. [11] for investigating the flow regimes in horizontal pipe, the transition between the moving bed regime and the suspension regime is easily found in the diagram of $\sigma_{pf} - \sigma_{col}$, where σ_{pf} decreases with the increase of σ_{col} in moving bed regime and increases with the increase of σ_{col} in suspension regime. It means that the two flow regimes in this paper are all corresponding to the suspension regime of the horizontal pipe. To explain the regime transition in this paper, we give the change of σ_{pf} and σ_{col} over Fr and St in Fig. 16b. σ_{pf} and σ_{col} all decrease with the increase of Fr, while the decreasing speed is different. For gravity-dominant regime, σ_{pf} and σ_{col} decrease very fast with Fr increasing. For particle-inertia-dominant regime, σ_{pf} and σ_{col} change little with Fr increasing. The particles are more likely to get suspended in particle-inertia-dominant regime, which reduces the chance of collisions between particles. This explains why σ_{col} is much smaller in particle-inertia-dominant regime than in gravity-dominant regime.

3.5. Pressure drop

The pressure drop is an important parameter for particle transportation in inclined pipe. It is related to the controlling dimensionless parameters, such as the particle volume fraction α_p, the Froude number Fr, the pipe inclination angle β, etc. As a result, we analyze the pressure drop in this section. We extract the pressure drop between the point (0 0 0.5) and (0 0 1.5) in the inclined pipe. The pressure drop is nondimensionlized by $\rho_f u_b^2$ as $\nabla p' = \nabla p/(\rho_f u_b^2)$. Fig. 17 gives the pressure drop under different dimensionless parameters (β, α_p, and Fr). It can be seen in Fig. 17a that the pressure drop increases with the increase in inclination angle β with approximately $0 < \beta < 60°$ and then decreases with β increasing. The maximum pressure drop occurs at around $\beta = 60°$. The simulation results are consistent with the work of Levy et al. [20] and Zhang et al. [57]. In addition, the pressure drop increases with the increase of the particle volume fraction α_p because the number of particles in the unit pipe section is higher for larger α_p, as shown in Fig. 17b. As the Froude number Fr increases, the gravitational effect weakens. So the pressure drop gradually decreases, as shown in Fig. 17c. For large Stokes number $St = 20$ and 35.6, the pressure drop decreases rapidly with Fr increasing from 5.7 to 11.4 due to the flow regime is the gravity-dominant regime. After the flow regime transiting

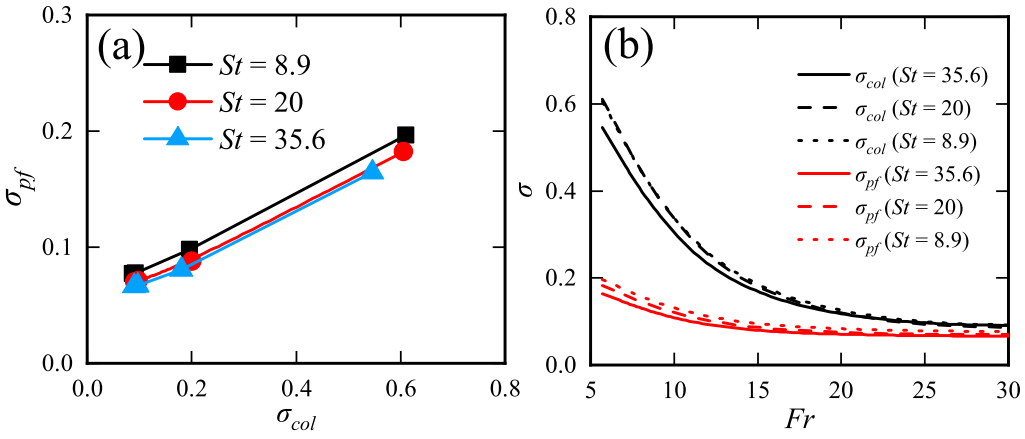

Fig. 16. The collision stress σ_{col} and the fluid–particle interaction stress σ_{pf} over different Stokes numbers St and Froude numbers Fr ($\beta = 45°$, and $\alpha_p = 0.1$).

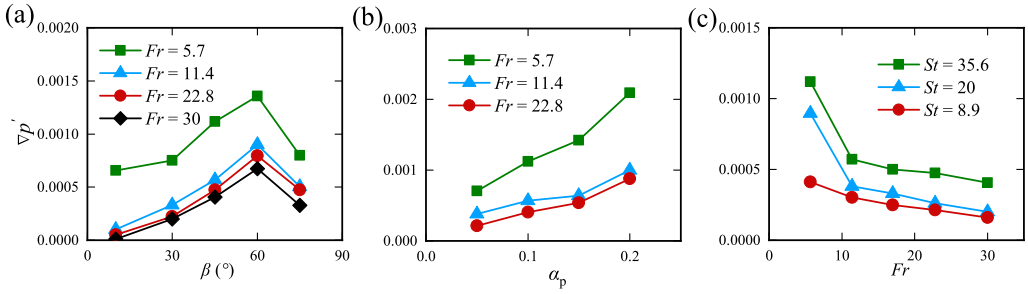

Fig. 17. The effects of (a) pipe inclination angle β, (b) particle volume fraction α_p, and (c) Froude number Fr on the pressure drop. The standard values of these dimensionless parameters are $St = 35.6$, $\beta = 45°$.

to the particle-inertia-dominant regime, the pressure drop decreases slowly with Fr increasing due to the weak effect of gravity.

4. Summary and conclusions

The flow regimes and their transition for dense particulate flows with coarse particles in inclined pipe are numerically investigated using the CFD-DEM, which is optimized for coarse particles. The validity of the CFD-DEM has been verified by the reasonable agreement between the simulated, analytical, and measured results in a fluidized bed case and a sediment transport process case.

Two different flow regimes are recognized for the dense particulate flows by the combination of Stokes number St (ratio of particle inertia to the fluid inertia) and Froude number Fr (ratio of fluid inertia to the gravity) in this paper. The flow behavior of the two regimes have been thoroughly analyzed. The two regimes are as follows: Gravity-dominant regime occurs when the influence of gravity is significant. This regime is identified for the cases $8.9 < St < 35.6$ and $5.7 < Fr < 11.4$ under the pipe inclination angle 45°. Most of the particles settle to the pipe bottom, which lead to the asymmetric of the profiles of the particle and fluid velocity as well as the particle volume fraction. The particle and fluid velocity are larger in the upper half of the pipe than that in the lower part. The velocity slip between the fluid and particles increase with an increase in the value of Stokes number St due to more momentum is needed from the fluid phase for large inertia particles. In addition, the influence of gravitational force on the velocities of the fluid and particles is stronger for small Fr than that for larger Fr. Particle-inertia-dominant regime corresponds to the effects of gravity being much weaker than that of particle inertia, resulting in the particles being distributed uniformly throughout the pipe domain. This regime is recognized for the cases $Fr > 22.8$. The particle and fluid velocity are approximately symmetric along the pipe cross section, where its value in the middle part of the pipe are larger than that in the bottom and top part. It is found that both the Stokes number St and Froude number St have little impact on the particle velocity distribution for very large Fr ($Fr > 22.8$). In addition, the particle volume fraction has little effect on the flow regimes. This may be because the particle volume fraction in this paper is in the dense phase range (0.05–0.20). Based on series numerical simulation, a new phase diagram for recognizing the transition between the two regimes is given under different pipe inclination angles. The transition area between the two regimes basically presents a linear distribution in $Fr - St$ diagram.

The temporal variations of the particle volume fraction and the particle velocity are also analyzed in this paper. Significant fluctuations are observed for both the particle volume fraction and particle velocity in the gravity-dominant regime due to the heterogeneous variable structure of the flow. The mechanism of fluctuations is discussed from the perspective of kinematic waves. The kinematic wave velocity is calculated from a linear relationship between the wave frequency and wave number under different controlling dimensionless parameters. The kinematic wave velocity increases with Froude number, inclination angle, and particle volume fraction increasing. Then, we analyze the transition mechanism between the two regimes. The pair probability is analyzed based on the particle positions. The microstructure of particles is more anisotropic and inhomogeneous for small Fr. The collision stress σ_{col} and fluid–particle interaction stress σ_{pf} are defined to illustrate the particle dynamics in different regimes, where σ_{col} and σ_{pf} are much smaller in particle-inertia-dominant regime than in gravity-dominant regime. At last, we investigate the pressure drop during the particle transportation. The pressure drop increases with the increase in inclination angle with approximately 0–60° and then decreases with inclination angle increasing.

CRediT authorship contribution statement

Yan Zhang: Methodology, Software, Validation, Data curation, Writing – original draft. **Wanlong Ren:** Validation, Investigation, Writing – review & editing. **Peng Li:** Methodology, Validation, Writing – review & editing. **Xuhui Zhang:** Software, Data curation, Funding acquisition, Writing – review & editing. **Xiaobing Lu:** Methodology, Supervision, Writing – review & editing.

Declaration of competing interest

The authors declare that they have no known competing financial interests or personal relationships that could have appeared to influence the work reported in this paper.

Data availability

Data will be made available on request.

Acknowledgments

This work was supported by the Strategic Priority Research Program of the Chinese Academy of Sciences [grant number XDA22000000]; the National Natural Science Foundation of China [grant number 12132018]; and the Youth Innovation Promotion Association of Chinese Academy of Sciences [grant number 2017027].

References

[1] H. Zhang, T. Li, Z. Huang, S. Kuang, A. Yu, Investigation on vertical plug formation of coarse particles in a non-mechanical feeder by cfd-dem coupling method, Powder Technol. 332 (2018) 79–89, http://dx.doi.org/10.1016/j.powtec.2018.03.055.

[2] M. Zhou, S. Wang, S. Kuang, K. Luo, J. Fan, A. Yu, Cfd-dem modelling of hydraulic conveying of solid particles in a vertical pipe, Powder Technol. 354 (2019) 893–905, http://dx.doi.org/10.1016/j.powtec.2019.07.015.

[3] T. Trewhela, J.M.N.T. Gray, C. Ancey, Large particle segregation in two-dimensional sheared granular flows, Phys. Rev. Fluids 6 (2021) 054302, http://dx.doi.org/10.1103/PhysRevFluids.6.054302.

[4] J. Su, C. Zhou, G. Ren, Z. Qiao, Y. Chen, Improving biomass mixture separation efficiency in multiple inclined channels of gas–solid fluidized bed: Cfd-dem simulation and orthogonal experiment, Powder Technol. 413 (2023) 118066, http://dx.doi.org/10.1016/j.powtec.2022.118066.

[5] Y. Dai, Y. Zhang, X. Li, Numerical and experimental investigations on pipeline internal solid–liquid mixed fluid for deep ocean mining, Ocean Eng. 220 (2021) 108411, http://dx.doi.org/10.1016/j.oceaneng.2020.108411.

[6] N.C. Cúñez, E.M. Franklin, Motion and clustering of bonded particles in narrow solid–liquid fluidized beds, Phys. Fluids 33 (2021) 023303, http://dx.doi.org/10.1063/5.0035718.

[7] Y. Zhang, X.B. Lu, X.H. Zhang, Numerical simulation on transportation behavior of dense coarse particles in vertical pipe with an optimized eulerian–lagrangian method, Phys. Fluids 34 (2022) 033305, http://dx.doi.org/10.1063/5.0084263.

[8] F.D. Cunez, N.C. Lima, E.M. Franklin, Motion and clustering of bonded particles in narrow solid–liquid fluidized beds, Phys. Fluids 33 (2021) 023303, http://dx.doi.org/10.1063/5.0035718.

[9] A. Bartosik, Validation of friction factor predictions in vertical slurry flows with coarse particles, J. Hydrol. Hydromech. 68 (2020) 119–127, http://dx.doi.org/10.2478/johh-2020-0005.

[10] E.W.C. Lim, Voidage waves in hydraulic conveying through narrow pipes, Chem. Eng. Sci. 62 (2007) 4529–4543, http://dx.doi.org/10.1016/j.ces.2007.05.034.

[11] M. Zhou, S. Kuang, K. Luo, R. Zou, S. Wang, A. Yu, Modeling and analysis of flow regimes in hydraulic conveying of coarse particles, Powder Technol. 373 (2020) 543–554, http://dx.doi.org/10.1016/j.powtec.2020.06.085.

[12] F. Ravelet, F. Bakir, S. Khelladi, R. Rey, Experimental study of hydraulic transport of large particles in horizontal pipes, Exp. Therm Fluid Sci. 45 (2013) 187–197, http://dx.doi.org/10.1016/j.expthermflusci.2012.11.003.

[13] P. Vlasák, Z. Chára, J. Krupička, Experimental investigation of coarse particles-water mixture flow in horizontal and inclined pipes, J. Hydrol. Hydromech. 62 (2014) 241–247, http://dx.doi.org/10.2478/johh-2014-0022.

[14] K. Wilson, A unified physically-based analysis of solid–liquid pipeline flow, in: Proc. Hydrotransport, BHRA Fluid Engineering Cranfield, UK, 1976, pp. 1–16.

[15] P. Doron, D. Granica, D. Barnea, Slurry flow in horizontal pipes—experimental and modeling, Int. J. Multiph. Flow. 13 (1987) 535–547, http://dx.doi.org/10.1016/0301-9322(87)90020-6.

[16] L. Liu, J. Yang, H. Lu, X. Tian, W. Lu, Numerical simulations on the motion of a heavy sphere in upward poiseuille flow, Ocean Eng. 172 (2019) 245–256, http://dx.doi.org/10.1016/j.oceaneng.2018.11.041.

[17] W. Chen, H.L. Xu, W.Y. Kong, F.qiong. Yang, Study on three-phase flow characteristics of natural gas hydrate pipeline transmission, Ocean Eng. 214 (2020b) 107727, http://dx.doi.org/10.1016/j.oceaneng.2020.107727.

[18] Q. Chen, T. Xiong, X. Zhang, P. Jiang, Study of the hydraulic transport of non-spherical particles in a pipeline based on the cfd-dem, Eng. Appl. Comput. Fluid Mech. 14 (2020a) 53–69, http://dx.doi.org/10.1080/19942060.2019.1683075.

[19] G.E. Klinzing, N.D. Rohatgi, C.A. Myler, S. Dhodapkar, A. Zaltash, M.P. Mathur, Pneumatic transport of solids in an inclined geometry, Can. J. Chem. Eng. 67 (1989) 237–244, http://dx.doi.org/10.1002/cjce.5450670210.

[20] A. Levy, T. Mooney, P. Marjanovic, D.J. Mason, A comparison of analytical and numerical models with experimental data for gas-solid flow through a straight pipe at different inclinations, Powder Technol. 93 (1997) 253–260, http://dx.doi.org/10.1016/S0032-5910(97)03280-4.

[21] P. Vlasak, Z. Chara, J. Konfrst, Flow behaviour and local concentration of coarse particles-water mixture in inclined pipes, J. Hydrol. Hydromech. 65 (2017) 183–191, http://dx.doi.org/10.1515/johh-2017-0001.

[22] A. Archibong-Eso, A.M. Aliyu, W. Yan, N.E. Okeke, Y.D. Baba, O. Fajemidupe, H. Yeung, Experimental study on sand transport characteristics in horizontal and inclined two-phase solid–liquid pipe flow, J. Pipeline Syst. Eng. Pract. 11 (2020) 04019050, http://dx.doi.org/10.1061/(ASCE)PS.1949-1204.0000427.

[23] S. Sundaresan, A. Ozel, J. Kolehmainen, Toward constitutive models for momentum, species, and energy transport in gas–particle flows, Annu. Rev. Chem. Biomol. Eng. 9 (2018) 61–81, http://dx.doi.org/10.1146/annurev-chembioeng-060817-084025.

[24] Y. Zhang, X. Lu, X. Zhang, P. Li, Numerical simulation on flow characteristics of large-scale submarine mudflow, Appl. Ocean Res. 108 (2021) 102524, http://dx.doi.org/10.1016/j.apor.2021.102524.

[25] Y. Yao, C.S. Criddle, O.B. Fringer, Competing flow and collision effects in a monodispersed liquid–solid fluidized bed at a moderate archimedes number, J. Fluid Mech. 927 (A28) (2021) http://dx.doi.org/10.1017/jfm.2021.780.

[26] D. Yang, Y. Xia, D. Wu, P. Chen, G. Zeng, X. Zhao, Numerical investigation of pipeline transport characteristics of slurry shield under gravel stratum, Tunn. Undergr. Space Technol. 71 (2018) 223–230, http://dx.doi.org/10.1016/j.tust.2017.08.011.

[27] H. Zhang, Y. Tan, D. Yang, F.X. Trias, S. Jiang, Y. Sheng, A. Oliva, Numerical investigation of the location of maximum erosive wear damage in elbow: Effect of slurry velocity, bend orientation and angle of elbow, Powder Technol. 217 (2012) 467–476, http://dx.doi.org/10.1016/j.powtec.2011.11.003.

[28] J. Chen, Y. Wang, X. Li, R. He, S. Han, Y. Chen, Erosion prediction of liquid-particle two-phase flow in pipeline elbows via cfd–dem coupling method, Powder Technol. 275 (2015) 182–187, http://dx.doi.org/10.1016/j.powtec.2014.12.057.

[29] M. Zhou, S. Kuang, F. Xiao, K. Luo, A. Yu, Cfd-dem analysis of hydraulic conveying bends: Interaction between pipe orientation and flow regime, Powder Technol. 392 (2021) 619–631, http://dx.doi.org/10.1016/j.powtec.2021.07.052.

[30] Z.Y. Zhou, S.B. Kuang, K.W. Chu, A.B. Yu, Discrete particle simulation of particle–fluid flow: model formulations and their applicability, J. Fluid Mech. 661 (2010) 482–510, http://dx.doi.org/10.1017/S002211201000306X.

[31] Y. Zhang, X.B. Lu, X.H. Zhang, An optimized eulerian–lagrangian method for two-phase flow with coarse particles: Implementation in open-source field operation and manipulation, verification, and validation, Phys. Fluids 33 (2021) 113307, http://dx.doi.org/10.1063/5.0067553.

[32] C. Fernandes, D. Semyonov, J.M. Ferrás, Validation of the cfd-dpm solver dpmfoam in openfoam through analytical, numerical and experimental comparisons, Granul. Matter 20 (2018) 1–18, http://dx.doi.org/10.1007/s10035-018-0834-x.

[33] R. Di Felice, The voidage function for fluid-particle interaction systems, Int. J. Multiph. Flow. 20 (1994) 153–159, http://dx.doi.org/10.1016/0301-9322(94)90011-6.

[34] J. Zhang, T. Li, H. Ström, B. Wang, T. Lø vås, A novel coupling method for unresolved cfd-dem modeling, Int. J. Heat Mass Transfer 203 (2023) 123817, http://dx.doi.org/10.1016/j.ijheatmasstransfer.2022.123817.

[35] R. Sun, H. Xiao, Diffusion-based coarse graining in hybrid continuum–discrete solvers: Theoretical formulation and a priori tests, Int. J. Multiph. Flow. 77 (2015a) 142–157, http://dx.doi.org/10.1016/j.ijmultiphaseflow.2015.08.014.

[36] R. Sun, H. Xiao, Diffusion-based coarse graining in hybrid continuum–discrete solvers: Applications in cfd–dem, Int. J. Multiph. Flow. 72 (2015b) 233–247, http://dx.doi.org/10.1016/j.ijmultiphaseflow.2015.02.014.

[37] Z. Wang, Y. Teng, M. Liu, A semi-resolved cfd–dem approach for particulate flows with kernel based approximation and hilbert curve based searching strategy, J. Comput. Phys. 384 (2019) 151–169, http://dx.doi.org/10.1016/j.jcp.2019.01.017.

[38] C. Goniva, C. Kloss, N.G. Deen, J.A. Kuipers, S. Pirker, Influence of rolling friction on single spout fluidized bed simulation, Particuology 10 (2012) 582–591, http://dx.doi.org/10.1016/j.partic.2012.05.002.

[39] R. Berger, C. Kloss, A. Kohlmeyer, S. Pirker, Hybrid parallelization of the liggghts open-source dem code, Powder Technol. 278 (2015) 234–247, http://dx.doi.org/10.1016/j.powtec.2015.03.019.

[40] R. Issa, A. Gosman, A. Watkins, The computation of compressible and incompressible recirculating flows by a non-iterative implicit scheme, J. Comput. Phys. 62 (1986) 66–82, http://dx.doi.org/10.1016/0021-9991(86)90100-2.
[41] S. Yang, K. Luo, J. Fan, K. Cen, Particle-scale investigation of the solid dispersion and residence properties in a 3-d spout-fluid bed, AIChE J. 60 (2014) 2788–2804, http://dx.doi.org/10.1002/aic.14494.
[42] N.C. Schnorr Filho, E.M. Franklin, Resolved cfd-dem simulations of the hydraulic conveying of coarse grains through a very-narrow elbow, Powder Technol. 395 (2022) 811–821, http://dx.doi.org/10.1016/j.powtec.2021.10.022.
[43] Y. Tsuji, T. Kawaguchi, T. Tanaka, Discrete particle simulation of two-dimensional fluidized bed, Powder Technol. 77 (1993) 79–87, http://dx.doi.org/10.1016/0032-5910(93)85010-7.
[44] M. Alletto, M. Breuer, Prediction of turbulent particle-laden flow in horizontal smooth and rough pipes inducing secondary flow, Int. J. Multiph. Flow. 55 (2013) 80–98, http://dx.doi.org/10.1016/j.ijmultiphaseflow.2013.04.009.
[45] X. Zhang, G.J. Nathan, Z.F. Tian, R.C. Chin, Flow regimes within horizontal particle-laden pipe flows, Int. J. Multiph. Flow. 143 (2021) 103748, http://dx.doi.org/10.1016/j.ijmultiphaseflow.2021.103748.
[46] C. Müller, D. Holland, A. Sederman, S. Scott, J. Dennis, L. Gladden, Granular temperature: Comparison of magnetic resonance measurements with discrete element model simulations, Powder Technol. 184 (2008) 241–253, http://dx.doi.org/10.1016/j.powtec.2007.11.046.
[47] C.R. Müller, S.A. Scott, D.J. Holland, B.C. Clarke, A.J. Sederman, J.S. Dennis, L.F. Gladden, Validation of a discrete element model using magnetic resonance measurements, Particuology 7 (2009) 297–306, http://dx.doi.org/10.1016/j.partic.2009.04.002.
[48] M. Wong, G. Parker, Reanalysis and correction of bed-load relation of meyer-peter and müller using their own database, J. Hydraul. Eng. 132 (2006) 1159–1168, http://dx.doi.org/10.1061/(ASCE)0733-9429(2006)132:11(1159).
[49] P. Nielsen, Coastal Bottom Boundary Layers and Sediment Transport, Vol. 4, World scientific, 1992.
[50] R. Sun, H. Xiao, Sedifoam: A general-purpose, open-source cfd–dem solver for particle-laden flow with emphasis on sediment transport, Comput. Geosci. 89 (2016) 207–219, http://dx.doi.org/10.1016/j.cageo.2016.01.011.
[51] M.W. Schmeeckle, Numerical simulation of turbulence and sediment transport of medium sand, J. Geophys. Res.: Earth Surf. 119 (2014) 1240–1262, http://dx.doi.org/10.1002/2013JF002911.
[52] T.C.W. Lau, G.J. Nathan, The effect of stokes number on particle velocity and concentration distributions in a well-characterised, turbulent, co-flowing two-phase jet, J. Fluid Mech. 809 (2016) 72–110, http://dx.doi.org/10.1017/jfm.2016.666.
[53] J.J. Derksen, S. Sundaresan, Direct numerical simulations of dense suspensions: wave instabilities in liquid-fluidized beds, J. Fluid Mech. 587 (2007) 303–336, http://dx.doi.org/10.1017/S0022112007007094.
[54] D.P. Willen, A.J. Sierakowski, G. Zhou, A. Prosperetti, Continuity waves in resolved-particle simulations of fluidized beds, Phys. Rev. Fluids 2 (2017) 114305, http://dx.doi.org/10.1103/PhysRevFluids.2.114305.
[55] J. van Wijk, A. Talmon, C. van Rhee, Stability of vertical hydraulic transport processes for deep ocean mining: An experimental study, Ocean Eng. 125 (2016) 203–213, http://dx.doi.org/10.1016/j.oceaneng.2016.08.018.
[56] X. Yin, D.L. Koch, Lattice-boltzmann simulation of finite reynolds number buoyancy-driven bubbly flows in periodic and wall-bounded domains, Phys. Fluids 20 (2008) 103304, http://dx.doi.org/10.1063/1.3001728.
[57] P. Zhang, T. Sheng, Z. Huang, Y. Yang, J. Sun, J. Wang, Y. Yang, C. Huang, Z. Huang, Experimental study of the effect of inclination angle on the minimum conveying velocity and the underlying mechanisms, AIChE J. 66 (2020) e16830, http://dx.doi.org/10.1002/aic.16830.